

Effects of volatile coatings on the laser-induced incandescence of soot

Ray P. Bambha · Mark A. Dansson ·
Paul E. Schrader · Hope A. Michelsen

Received: 30 November 2012 / Accepted: 22 April 2013 / Published online: 21 May 2013
© The Author(s) 2013. This article is published with open access at Springerlink.com

Abstract We have measured time-resolved laser-induced incandescence (LII) from combustion-generated mature soot extracted from a burner and (1) coated with oleic acid or (2) coated with oleic acid and then thermally denuded using a thermodenuder. The soot samples were size selected using a differential mobility analyzer and characterized with a scanning mobility particle sizer, centrifugal particle mass analyzer, and transmission electron microscope. The results demonstrate a strong influence of coatings on the magnitude and temporal evolution of the LII signal. For coated particles, higher laser fluences are required to reach signal levels comparable to those of uncoated particles. The peak LII curve is shifted to increasingly higher fluences with increasing coating thickness until this effect saturates at a coating thickness of $\sim 75\%$ by mass. These effects are predominantly attributable to the additional energy needed to vaporize the coating while heating the particle. LII signals are higher and signal decay rates are significantly slower for thermally denuded particles relative to coated or uncoated particles, particularly at low and intermediate laser fluences. Our results suggest negligible coating enhancement in absorption cross-section for combustion-generated soot at the laser fluences used. Apparent enhancement in absorption with restructuring may be caused by less conductive cooling.

1 Introduction

Current climate models suggest that black-carbon particles, that is, soot particles, contribute significantly to global warming and climate change because they absorb strongly in the visible and infrared regions of the solar spectrum [1]. Estimates of their impact on climate have large uncertainties, however, because their optical properties are not well represented in climate models, and their atmospheric abundance and distribution are not well known [2]. Reducing these uncertainties will require a detailed understanding of their optical properties, reliable measurements of their atmospheric abundance, and better estimates of their emissions. Reduction in soot emissions has been proposed as a near-term climate-change mitigation approach [3]. This mitigation approach will require a better understanding of soot formation processes during combustion and reliable measurements of soot in combustors and exhaust streams.

Laser-induced incandescence (LII) is a technique that has been developed over decades to measure soot particle abundances and physical properties in combustors, such as engines [4–10] and flames [11–17], and in combustion exhaust streams [18–21]. More recently, it has been applied to measurements of ambient atmospheric black-carbon particles [22–29]. The implementation of this technique involves heating soot particles in an intense laser field and measuring the incandescence from the hot particles. The magnitude of the signal is correlated with the particle volume fraction or mass if the density is constant (see [30] and references therein).

Soot particle coatings can have a strong effect on the optical properties of the particle. A non-absorptive coating on a spherical soot particle is predicted to increase the scattering cross-section, particularly forward scattering [21,

R. P. Bambha · M. A. Dansson · P. E. Schrader ·
H. A. Michelsen (✉)
Combustion Research Facility, Sandia National Labs,
Livermore, CA, USA
e-mail: hamiche@sandia.gov

31–33]. Such a coating is also expected to increase the absorption cross-section because of a refractive focusing effect of the coating [32–39]. These effects will have a significant influence on (1) the impact of black carbon on the Earth's climate and (2) the application of optical techniques, such as LII, to measure it under conditions in which it is expected to be coated, for example, in combustors, exhaust streams, and the atmosphere.

Coatings can also influence soot particle morphology, which has additional effects on its optical properties. Mature uncoated soot aggregates have a dendritic, branched-chain morphology described by a fractal dimension of ~ 1.7 to 1.9 [40–51]. Numerous studies have shown that this aggregate morphology can become substantially compressed when the particles are coated with oxygenated hydrocarbons [48, 51–61] or sulfuric acid [21, 56, 62–64]. This morphology restructuring may persist even when the coating is removed in a thermodenuder [51, 53, 55, 56, 60, 63, 64]. We recently showed that, for oleic acid coatings, the restructuring is largely reversible if the coating is removed by laser irradiation but is irreversible if the coating is removed in a thermodenuder [51]. The particle maintains its restructured morphology after the coating is removed in a thermodenuder, even if the particle is laser heated after the thermodenuder.

The predicted effect of the coating-induced restructuring of the particle on its optical properties is unclear; some theories predict that the increased scattering interactions between primary particles should lead to an increase in the scattering cross-section with increasing fractal dimension [65, 66], whereas other studies indicate that the scattering cross-section should decrease with fractal dimension because of either the reduction in the aggregate size or destructive interference of multiply scattered waves at the core of the aggregate [21, 32, 45, 49]. The coating-induced particle compression is predicted to reduce the absorption cross-section for particles with a fractal dimension below ~ 2 because of increased shielding of the primary particles [32, 45, 67]. At fractal dimensions above 2, the absorption cross-section is predicted to increase with fractal dimension [65]. Over the range of fractal dimension change induced by coatings (e.g., 1.78–2.50 [49], 1.7–2.7 [21], 1.9–2.1 [54], 1.72–1.87 [48], 1.88–2.34 [51]), however, the calculated dependence of the absorption cross-section on fractal dimension is not strong [65, 67, 68].

The predicted net effect of volatile coatings on soot optical properties is an enhancement in both scattering and absorption cross-sections [21]. These predictions are supported by experimental studies, which have demonstrated large enhancements in soot scattering and absorption cross-sections attributable to coatings [21, 50, 54–56, 59, 62, 63, 69, 70].

Volatile coatings can also have an effect on the radiative emission from laser-heated soot and graphite particles and, thus, on LII signals [21, 50, 71]. Considerable work has been devoted to modeling the particle laser heating, cooling, and mass loss processes in an attempt to understand and predict the effects of ambient conditions and particle characteristics on the LII signal (see [72] and references therein). Relatively little work, however, has addressed the impact of volatile coatings on LII. Using an energy- and mass-balance model, Michelsen and co-workers [21, 73] predicted that, at low laser fluences from a nanosecond pulsed laser, volatile coatings will have a large effect on the magnitude of the LII signal, but this effect nearly disappears at high laser fluences. This behavior is caused by the requirement for additional energy to vaporize the coating before the core refractory particle can reach its peak temperature, which determines the peak LII signal. At laser fluences high enough to drive off the coating and heat the particle to sublimation temperatures, the peak temperature of $\sim 4,450$ K will be reached whether the particle is initially coated or not, and the peak LII signal will thus be insensitive to particle coating. They confirmed these model predictions with preliminary experimental studies of coatings of sulfuric acid on mature soot extracted from a flame [73]. The results are inconsistent with the experimental results of [74], which indicate that differences in LII signal between coated and uncoated particles are insignificant at all laser intensities.

Moteki and Kondo [71] used an approach similar to that of Michelsen and co-workers [21, 73] to model LII signal from coated graphite particles. Moteki and Kondo [71] modelled an experimental configuration in which a particle drifts through a CW laser beam. Their system was similar to that of Michelsen and co-workers [21, 73] for a high-intensity laser (~ 3 to 30 J/cm²) with a long pulse duration (~ 20 to 30 μ s). Their model predicted that the evaporative heating of the particle coating should delay the appearance of the LII signal. This result is qualitatively consistent with the experimental results of Moteki and Kondo [71] and Slowik et al. [50], which showed that the delay of the onset of the LII signal, once the particle has intersected with the laser beam, increased with increasing coating thickness.

None of these studies directly addressed the impact of coating-induced restructuring of the particle. Several studies have targeted the effects of aggregate size on LII signals via its influence on particle conductive-cooling rates [75–79] and optical properties [80, 81], but none of these studies has addressed the effects of fractal dimension on LII.

In this paper, we present results of experiments focused on determining the effects of coatings of oleic acid on the magnitude and temporal response of LII from combustion-

generated mature soot particles. Our results demonstrate a strong dependence of the LII signal magnitude on particle coating at low and intermediate laser fluences. This result is consistent with the predictions of Michelsen and co-workers [21, 73] but inconsistent with the results of Schwarz et al. [74]. The LII excitation curve (peak LII vs fluence) shifts to higher fluence with increasing coating at moderate coating thickness but shifts back to lower fluences with heavy coating thicknesses. In addition, the rising edge of our LII temporal profiles is sensitive to coating thickness, that is, the onset of the signal for coated particles appears later in time than for uncoated particles. This result is qualitatively similar to the results of Moteki and Kondo [71] and Slowik et al. [50]. The decay rate of the LII signal also appears to be sensitive to particle coating when the particle has been thermally denuded, but the main effect observed is likely attributable to a coating-induced increase in the fractal dimension of the particle and its effects on the conductive-cooling rate.

2 Experimental approach

2.1 Soot generation, coating application, and thermal denuding

A schematic diagram of the experimental apparatus is shown in Fig. 1. We generated soot in an ethylene–air flame from a coflow diffusion burner. The burner had a central fuel nozzle (0.5 cm in diameter) protruding 15 mm above a honeycomb structure (44 mm in diameter), which conducted the air coflow [43, 82, 83]. A mass flow controller (MKS Type 1479A) held the ethylene flow rate at 0.220 standard liters per minute (relative to 0 °C and 760 Torr) (slm-MKS). A second flow controller (MKS Type 1559A) held the air coflow at 14 slm-MKS. A brass mesh tube of 1-cm diameter surrounded the flame to a height of 25 mm and helped to stabilize the flame. The flame and air coflow were completely enclosed in a modular flow tube constructed from 50-mm ID tubing components (Kwik-Flange NW50). The visible flame height in the flow tube was approximately 100 mm. The flame was cut at ~65-mm height above the burner by a horizontal nitrogen cross-flow of 50 slm-MKS, which quenched the combustion and carried the soot to the sampling tube approximately 45 cm downstream. A Venturi pump (Vaccon JS-40UM) extracted the soot from the center of the cross-flow tube through a 0.25-inch stainless steel tube with a sample flow rate of 0.38 slm-MKS and a dilution flow rate of 1.2 slm-MKS, which corresponded to a dilution ratio of ~4:1. A differential mobility analyzer (DMA) (TSI 3081) selected soot in a narrow size range for use in the subsequent coating, denuding, and measurement

sections. The DMA was set to select aggregates of mobility diameter 150 nm using a sample flow rate of 0.2 standard liters per minute (relative to 21 °C and 1 bar) (slm-TSI) and a sheath flow of 2.0 slm-TSI.

The coating condenser consisted of a straight section of 50-mm ID stainless steel tubing 14 cm long with tapered ends that allowed the particles to flow through continuously to mitigate the effects of multiple residence times. The condenser was wrapped in heating tape and insulated, and a type-K thermocouple provided the feedback for a temperature controller. The coating material used in the experiments was oleic acid ($\geq 99\%$, Sigma Aldrich). The temperature of the oleic acid was measured with a thermocouple inside the chamber immersed in the liquid. The flow rate of the aerosol was 0.200 slm-MKS for all experiments, and the volume of the chamber was 400 ml, which resulted in a residence time of approximately 2 min in the coating chamber. Immediately downstream of the coating chamber, a room temperature denuder containing activated carbon strips (Sunset Laboratory) trapped coating vapor leaving the condenser but allowed the coated particles to pass.

Coatings could be removed from the particles using a thermodenuder. Our thermodenuder design achieved the two important criteria suggested by Fierz et al. [84] of avoiding strong temperature gradients and maintaining elevated gas temperatures in the absorption section. We achieved the desired behavior using two temperature-controlled sections as opposed to the three sections in the Fierz et al. [84] design. The overall length of the thermodenuder was 100 cm with the initial 70 cm heated in two zones, each 35 cm in length. The aerosol flowed through 12-mm ID tubing, the first 40 cm of which was solid-walled stainless steel tubing, and the last 60 cm of the tubing was fine stainless steel mesh surrounded by activated charcoal contained within a 25-mm ID stainless steel tube. The initial 90 cm of the denuder was surrounded by 50-mm-thick fiberglass insulation, and over the last 10 cm, the stainless steel tubing was left exposed. In the initial heated section intended to desorb coatings, the tubing was heated to 410 °C, while the second heated section, which included 30 cm of the activated carbon, was heated to 170 °C. The peak temperature in the aerosol stream was 400 °C, approximately in the middle of the initial heated section, and the temperature gradually transitioned down to approximately room temperature at the exit of the denuder.

2.2 Particle characterization by SMPS, CPMA, and TEM

Mobility size distributions were recorded using a scanning mobility particle sizer (SMPS), which consisted of an electrostatic classifier (TSI 3080 with TSI 3081 DMA) and the condensation particle counter controlled by a computer.

The sample flow in the SMPS was 0.2 slm-TSI, and the sheath flow was 2.0 slm-TSI. The input and output flows of the DMA were balanced, giving a theoretical mobility resolution of 10 % of the measured mobility size [85]. An impactor with a 0.0457-mm orifice at the SMPS limited the maximum sampled particle diameters to approximately 800 nm.

Particle masses were monitored with a centrifugal particle mass analyzer (CPMA) (Cambustion). Results of the mass measurements are summarized here; more details are given in [51].

Soot particles were collected on TEM grids downstream of the condenser, denuder, and laser-heating cell. The grids were a copper mesh substrate covered with a layer of Formvar and stabilized with silicon monoxide (Ted Pella, 01830). The TEM grids were analyzed using a JEOL 1200 EX TEM (120 kV). The images were collected at a magnification of 250,000 using a CCD camera with a scaling of approximately 0.4 nm/pixel.

2.3 Laser-induced incandescence measurements

The optical arrangement used for LII is shown in Fig. 1. A Nd:YAG laser (Continuum NY81C) generated 17 ns

(full width at half max) unseeded pulses at 1064 nm and a repetition rate of 10 Hz. A top-hat intensity distribution was generated by placing a 3-mm iris in a uniform section of the ~ 5 -mm laser output beam. The top-hat profile was relay imaged and demagnified to 1-mm diameter using two lenses (152.5- and 50-cm focal length). A camera (DataRay WinCam-D) profiled the beam, as shown in Fig. 2, and the intensity profiles were measured and adjusted to have root-mean-squared variations of approximately 14 % in the soot LII detection region. A first thin-film polarizer ensured the beam had a well-defined vertical polarization, and the power was adjusted by rotation of a half-wave plate, which was followed by two fixed thin-film polarizers. The average laser pulse energy was measured using a power meter (Coherent PM3 or PS19).

The laser irradiation of the soot for LII was performed in a flow cell shown in Fig. 1. Windows on the cell provided optical access for the LII measurements and the laser input. Soot entered the cell through a 5-mm ID tube and flowed through the center of the cell surrounded by a sheath of clean air along a path perpendicular to the laser beam. A lens (25-mm focal length) placed one focal distance from the center of the cell collected the incandescence and directed it through two filters (Schott RG610 long-pass and

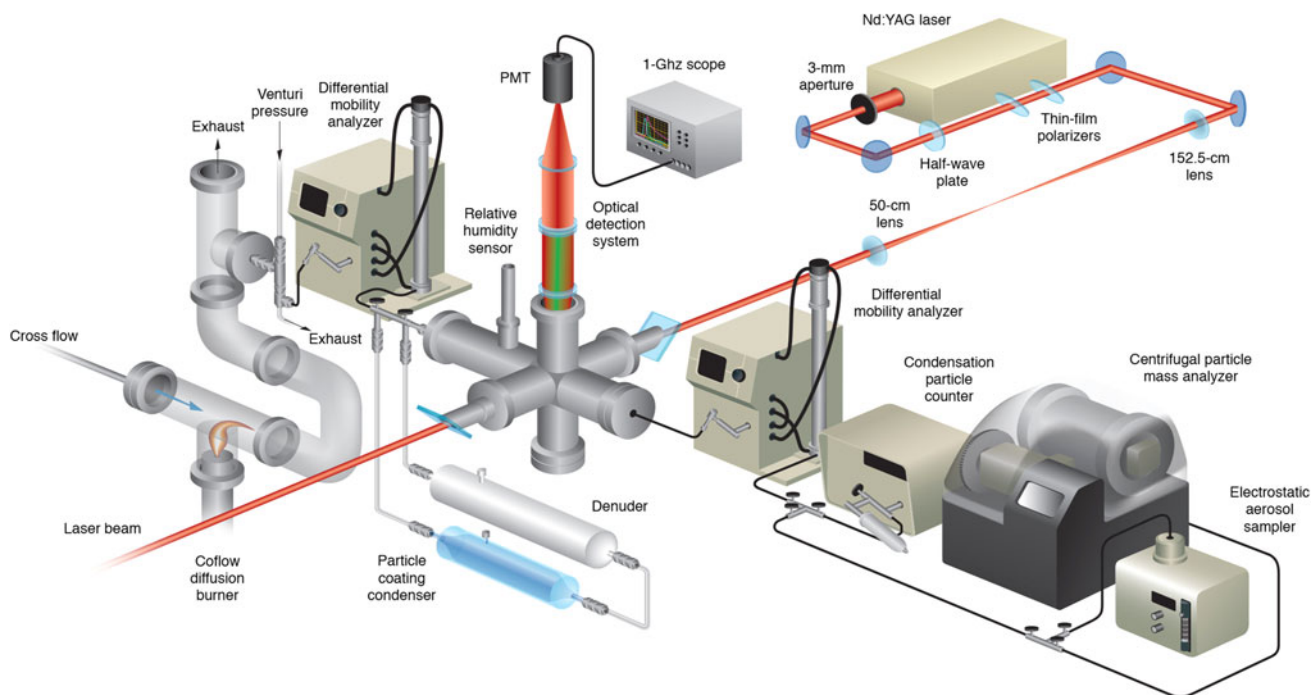


Fig. 1 Illustration of the experimental setup. Soot was generated in a coflow diffusion ethylene–air flame at atmospheric pressure. Combustion was quenched with a cross-flow of nitrogen. Part of the flow was extracted and sent through a DMA for size selection. The size-selected soot could be sent through a condenser and coated with oleic acid. The coated or uncoated soot could also be sent through a thermodenuder to

remove coating. The uncoated, coated, or denuded soot was sent into an optical cell, where the particles were heated with a pulsed 1,064-nm laser beam with a homogeneous spatial profile. The LII signal was detected with a photomultiplier tube attached to an oscilloscope. The particles were characterized by SMPS measurements of mobility size, CPMA measurements of mass, and TEM imaging of morphology

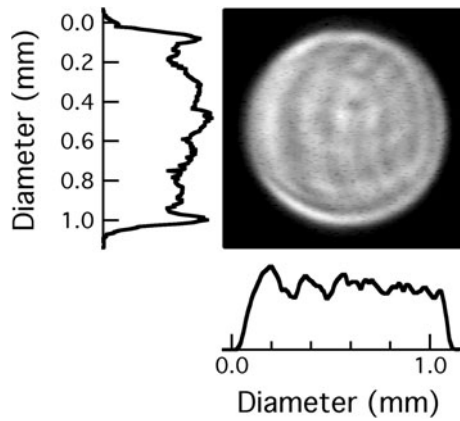


Fig. 2 Laser beam spatial profile. The image of the 1,064-nm laser beam was taken using a camera with a pixel size of $6.7 \mu\text{m} \times 6.7 \mu\text{m}$. The beam diameter was 0.99 mm with a spatial variability of $\sim 14\%$ (one standard deviation) over the entire beam profile. The lines represent *vertical* and *horizontal cross-sections* through the beam profile shown

Thorlabs FES0900-1 900 nm short-pass) to a second lens (75 mm focal length) that imaged the incandescence onto the face of a photomultiplier tube (PMT) (Hamamatsu R7400-20). The filters blocked the 1,064-nm laser scatter and passed incandescence from 610 to 900 nm.

3 Analysis approach

3.1 Inference of maximum particle temperatures

Maximum particle temperatures were estimated from the peak LII signal using an expression based on the Planck function. The LII signal from X aggregate particles at the detection wavelength λ_s is given by the Planck function modified by the emissivity to correct for deviations from perfect blackbody emission, that is,

$$S = XN \frac{2\pi^2 d_p^3 hc^2 E(m)}{\lambda_s^6} \frac{1}{\exp\left(\frac{hc}{\lambda_s kT}\right) - 1} \Omega \Sigma_\lambda, \tag{1}$$

where N is the number of primary particles in the aggregate, d_p is the primary-particle diameter, h is the Planck constant, c is the speed of light, and k is the Boltzmann constant. The spectral response and efficiency of the detector are represented by Σ_λ . The solid angle element Ω is determined by the detector configuration, which, for cylindrically symmetric collection optics and detector, is given by

$$\Omega = 2\pi(1 - \cos\theta), \tag{2}$$

where θ is the acceptance angle of the detection system. The dimensionless refractive-index function for absorption $E(m)$ is given by

$$E(m) = -\text{Im}\left(\frac{m^2 - 1}{m^2 + 2}\right) = \frac{6nk}{(n^2 - k^2 + 2)^2 + 4n^2k^2} \tag{3}$$

for a complex refractive index $m = n - ki$. $E(m)$ is calculated to be 0.373 using a value for the refractive index of $1.75 - 1.03i$ measured by Williams et al. [86] at 635 nm in Eq. (3). Previous work has suggested deviations from the $1/\lambda$ dependence of the emissivity [87–92], which can be accounted for by assuming a wavelength dependence for $E(m)$. The wavelength dependence derived from the work of Köylü and Faeth [88, 93] can be expressed as

$$E(m) = \frac{\lambda_s^{1-\xi} \beta}{6\pi}, \tag{4}$$

where $\xi = 0.83$ [88]. A value for the scaling factor β of $36.34 \text{ cm}^{-0.17}$ allows $E(m)$ in Eq. (4) to match the value of $E(m)$ given by Eq. (3) with the refractive index from Williams et al. [86] at 635 nm.

We used the same detection optics for all of the experiments described here, which ensured that λ_s , Ω , and Σ_λ did not change between measurements. We also used the same soot generation and size-selection process. Monitoring of particle characteristics using TEM imaging confirmed that the primary-particle size of the core soot particles did not vary over the course of these measurements, and monitoring using an SMPS and a CPMA ensured that the aggregate size did not change. We can also assume that the fine structure of the core soot particles is unlikely to vary during these experiments, and therefore, the values of $E(m)$ and the sublimation temperature T_{sub} should not change. As long as the number of particles in the detection volume X does not vary over a fluence sweep (a scan in fluence), we can normalize the signal over the entire fluence sweep such that the peak LII signal at high fluences is normalized to one.

Given the above conditions, Eq. (1) can be simplified to

$$S = \frac{A}{\exp\left(\frac{B}{T}\right) - 1} - C, \tag{5}$$

where $B = hc/\lambda_s k$. Our peak LII signal is scaled from 0 at room temperature to a maximum of 1 at high fluence. C accounts for scaling the signal to zero at 298 K. A encompasses a host of constants; for our normalized LII signal, assuming that the particle does not surpass T_{sub} ($\sim 4,450 \text{ K}$) [94] at high fluences, A is given by

$$A = \left[\frac{1}{\exp\left(\frac{B}{4450}\right) - 1} - \frac{1}{\exp\left(\frac{B}{298}\right) - 1} \right]^{-1}, \tag{6}$$

which equals 113.6 for $\lambda = 682 \text{ nm}$. Likewise C is given by

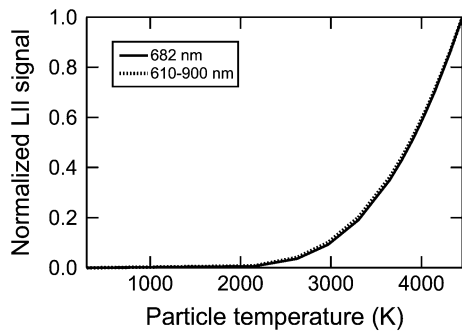


Fig. 3 Temperature dependence of the LII signal. The solid curve represents the signal calculated using Eq. (5), which corresponds to detection at a single wavelength. The calculated signal is normalized to unity at a temperature of 4,450 K and to zero at 298 K. The dotted curve represents the similarly normalized signal calculated using Eq. (1) integrated over a wavelength range of 610–900 nm

$$C = \frac{A}{\exp\left(\frac{B}{298}\right) - 1}, \quad (7)$$

which equals 2.019×10^{-29} for $\lambda = 682$ nm. Figure 3 shows a plot of the signal calculated using Eq. (5) as a function of temperature. This equation estimates the signal at a single wavelength (682 nm). Our experiments, however, were performed with broadband collection from 610 nm to the PMT wavelength limit of ~ 890 nm. Figure 3 also shows the signal calculated using Eq. (1) with the true PMT spectral response function and integrated over the wavelength range of 610–900 nm. The comparison in Fig. 3 demonstrates that the approximation of single-wavelength detection leads to a very small systematic error in calculated signal.

The maximum particle temperature T_{\max} at a particular fluence can then be calculated from the peak LII signal S_{pk} by solving Eq. (5) for temperature, which yields

$$T_{\max} = \frac{B}{\ln\left(\frac{A}{S_{\text{pk}} + C} + 1\right)}. \quad (8)$$

The small bias in calculated signal caused by the approximation of single-wavelength detection (Fig. 3) corresponds to a bias in the inferred temperature of less than 50 K.

3.2 Factors influencing maximum particle temperature

The particle-heating rate and the ultimate temperature reached by the particle are controlled by the balance of gain of energy as the particle absorbs laser radiation or is oxidized with the loss of energy by conduction, radiation, core sublimation, and coating vaporization. During the laser pulse, the rate of heating by absorption greatly exceeds the oxidative heating rate and the conductive and radiative cooling rates by orders of magnitude at atmospheric

pressure [93]. Sublimation rates are negligible at low fluences. Neglecting oxidative heating and conductive, radiative, and evaporative (core sublimation) cooling, the energy-balance equation can be approximated by

$$[Mc_s(T) + M_{\text{coat}}c_{\text{coat}}(T)] \frac{dT}{dt} = \dot{Q}_{\text{abs}} - \dot{Q}_{\text{coat}}, \quad (9)$$

where M is the particle mass, c_s is the specific heat of the core particle, M_{coat} is the mass of the particle coating, c_{coat} is the specific heat of the coating (2.046 J/g K for oleic acid), T is the particle temperature, and t is time. \dot{Q}_{abs} is the heating rate by absorption of laser radiation and is given by

$$\dot{Q}_{\text{abs}} = \sigma_{\text{abs}} F_L q_n(t) \quad (10)$$

where σ_{abs} is the absorption cross-section, F_L is the laser fluence, and $q_n(t)$ is the normalized laser temporal profile, which yields a value of one when integrated over the laser pulse in time. \dot{Q}_{coat} is the cooling rate by evaporation of the volatile coating and is given by

$$\dot{Q}_{\text{coat}} = \frac{\Delta H_{\text{coat}}}{W_{\text{coat}}} \frac{dM_{\text{coat}}}{dt}, \quad (11)$$

where ΔH_{coat} is the enthalpy of vaporization of the coating at its boiling point (1.356×10^5 J/mol for oleic acid [95]), and W_{coat} is the molecular weight of the coating (282.47 g/mol for oleic acid). Integrating Eq. (9) over the laser pulse gives

$$M \int_{T_0}^{T_{\max}} c_s dT + M_{\text{vap}} c_{\text{coat}} (T_{\text{boil}} - T_0) = \sigma_{\text{abs}} F_L - M_{\text{vap}} \frac{\Delta H_{\text{coat}}}{W_{\text{coat}}}, \quad (12)$$

assuming that some amount of coating M_{vap} vaporizes after being heated from the initial particle temperature T_0 to the boiling point T_{boil} (658.5 K for oleic acid). If all of the coating vaporizes, $M_{\text{vap}} = M_{\text{coat}}$. Assuming that c_s is approximately constant with temperature, performing the integration, and rearranging Eq. (12) yields

$$T_{\max} = \frac{\sigma_{\text{abs}} F_L}{M c_s} - \frac{M_{\text{vap}}}{M c_s} \left[\frac{\Delta H_{\text{coat}}}{W_{\text{coat}}} + c_{\text{coat}} (T_{\text{boil}} - T_0) \right] + T_0. \quad (13)$$

In these studies, the average coating mass M_{coat} was determined by integrating over the entire mass distribution for the coated particles.

3.3 Inferring coating effects on LII signal and absorption cross-section

Particles with the same volume fraction, size, fine structure, and morphology that reach the same T_{\max} will produce the

same maximum LII signal for a particular detection system. For fluences at which coated particles give the same peak LII signal as uncoated particles, from Eq. (13) we can assume that

$$\frac{\sigma_{\text{coat}} F_L(\text{Coated})}{M c_s} - \frac{M_{\text{vap}}}{M c_s} \left[\frac{\Delta H_{\text{coat}}}{W_{\text{coat}}} + c_{\text{coat}}(T_{\text{boil}} - T_0) \right] = \frac{\sigma_{\text{uncoat}} F_L(\text{Uncoated})}{M c_s}, \tag{14}$$

where $F_L(\text{Coated})$ gives the same peak LII signal for coated particles as does $F_L(\text{Uncoated})$ for uncoated particles, σ_{uncoat} is the absorption cross-section for uncoated particles, and σ_{coat} is the corresponding absorption cross-section for coated particles. Simplifying and rearranging Eq. (14) yield

$$F_L(\text{Coated}) = \frac{\sigma_{\text{uncoat}}}{\sigma_{\text{coat}}} F_L(\text{Uncoated}) + \frac{M_{\text{vap}}}{\sigma_{\text{coat}}} \Gamma, \tag{15}$$

where

$$\Gamma = \left[\frac{\Delta H_{\text{coat}}}{W_{\text{coat}}} + c_{\text{coat}}(T_{\text{boil}} - T_0) \right]. \tag{16}$$

Equation (15) suggests that a plot of $F_L(\text{Coated})$ as a function of $F_L(\text{Uncoated})$ will give a line with a slope that depends on the coating enhancement for absorption, that is,

$$\frac{1}{\text{Slope}} = \frac{\sigma_{\text{coat}}}{\sigma_{\text{uncoat}}}. \tag{17}$$

From the ratio of the intercept to the slope, we can estimate how much coating was evaporated from the particle, that is,

$$M_{\text{vap}} = \frac{\text{Intercept}}{\text{Slope}} \frac{\sigma_{\text{uncoat}}}{\Gamma}. \tag{18}$$

For oleic acid at $T_0 = 298$ K, $\Gamma = 1217.6$ J/g. We can estimate σ_{uncoat} using the equation for a particle in the Rayleigh regime [45], that is,

$$\sigma_{\text{uncoat}} = N \frac{\pi^2 d_p^3 E(m)}{\lambda_L}, \tag{19}$$

where λ_L is the laser wavelength (1064 nm), and d_p is the primary-particle diameter (11 nm for this study). The number of primary particles N can be determined according to

$$N = \frac{6M}{\pi d_p^3 \rho}, \tag{20}$$

where the average uncoated particle mass over the entire mass distribution was determined from CPMA measurements to be 1.321 fg [51], and ρ is the density for polycrystalline graphite assumed to be 1.8 g/cm³. Combining Eqs. (4), (19), and (20) gives an expression for the uncoated aggregate absorption cross-section in terms of the uncoated aggregate mass, that is,

$$\sigma_{\text{uncoat}} = \frac{\beta M}{\rho \lambda_L^2}, \tag{21}$$

which gives an average value for σ_{uncoat} of 5.29×10^{-11} cm² at 1,064 nm.

4 Results and discussion

4.1 Effects of coatings on the peak LII signal

Coating the particles with oleic acid has a significant effect on the magnitude of the LII signal at low and moderate laser fluences ($< \sim 0.4$ J/cm²). Figure 4 shows the laser fluence dependence of the peak of the LII temporal profiles at low to moderate particle coating thicknesses (Fig. 4a) and at moderate to high coating thicknesses (Fig. 4b). At any fluence below 0.4 J/cm², the LII signal for the uncoated particles is significantly higher than that associated with the coated particles. The difference between the signals from coated and uncoated particles depends on laser fluence and coating thickness. These differences are qualitatively consistent with the predictions of Witze et al. [21] and are at least partially attributable to the increase in the energy needed to vaporize the volatile coating. The laser energy required to heat the core particle to a particular temperature requires the additional energy needed to vaporize the coating, which increases with the amount of coating, and the peak LII excitation curves are thus shifted to higher laser fluence, with increasing coating thickness. Figure 4a shows that, as the coating increases from low to moderate coating thicknesses, the amount of additional energy needed to desorb the coating also increases. Table 1 gives the coating mass and coating mass fraction for selected condenser temperatures [51].

At some moderate coating thickness (condenser temperature of ~ 85 °C), the peak LII excitation curves stop shifting to higher fluences. Figure 4b shows that at higher coating thicknesses, the curves start shifting to lower fluence. These effects are summarized in Fig. 5, which shows the difference between the fluence needed to heat the coated particles and the fluence needed to heat the uncoated particles for different amounts of coating as a function of normalized peak LII signal, that is, the y-axis on Fig. 4. The shift increases for condenser temperatures up to 85 °C and decreases for condenser temperatures above 90 °C. The denuded peaks tend to have a negative shift.

These effects can be analyzed with respect to the particle temperature, which is directly related to the LII signal. Figure 6a shows the laser fluence dependence of the peak of the LII temporal profiles on a linear scale and the temperatures inferred from these data using Eq. (8). The

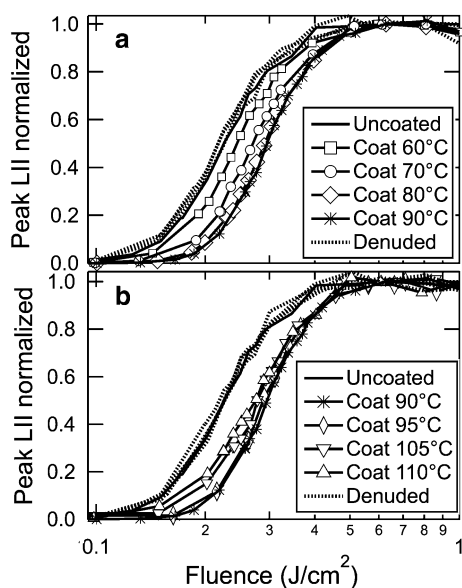


Fig. 4 Fluence dependence of the peak LII signal. The normalized peak of the LII temporal profile is plotted relative to laser fluence on a log scale for **a** low to moderate coating thickness and **b** high coating thickness, as indicated in the legend. The coating masses and mass fractions corresponding to the condenser temperatures shown in the legend are given in Table 1. All curves corresponding to the denuded particles are indicated by dotted lines

Table 1 Summary of coating mass

Coating	Condenser temperature (°C)	Coating mass* (fg)	Coating mass uncertainty (fg)*	Coating mass fraction
Uncoated*	20	0.000		0.00
Very light	40	0.030	0.200	0.02
Light	60	0.336	0.223	0.20
Moderately light	70	1.004	0.273	0.43
Moderate	80	2.457	0.382	0.65
Moderately heavy	90	8.272	0.819	0.86
Heavy	95	15.339	1.349	0.92
Very heavy	105	48.150	3.809	0.97
Extremely heavy	110	91.393	7.053	0.99

* The average mass of the uncoated particle was 1.321 fg. Values are integrated over all three modes of the mass distributions presented in [51] with 1σ standard deviation

maximum particle temperature increases approximately linearly with fluence at low and intermediate fluences, as suggested by Eq. (13) and shown in Fig. 6b. The peak LII signal increases nonlinearly with temperature and hence laser fluence, at these fluences, as indicated by Eqs. (1) and (5). The maximum temperature and peak LII signal are predominantly determined by the initial particle temperature, the amount of energy absorbed by the particle during the laser pulse, the amount of energy needed to desorb the volatile coating, the amount of energy lost by heat

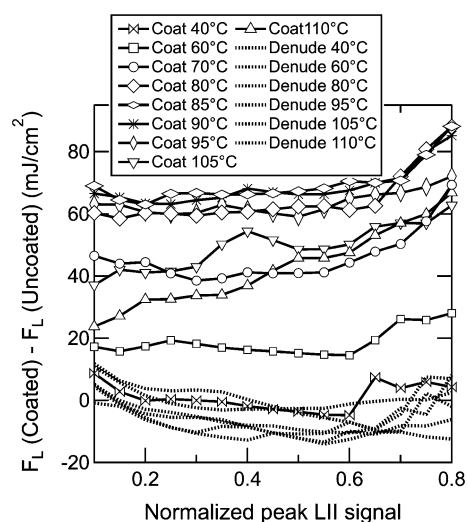


Fig. 5 Fluence shift of the peak LII excitation curves plotted against the normalized peak LII signal. This shift represents the increase in fluence required to heat coated particles to a comparable temperature as uncoated particles. For measurements with the same normalized LII signal (x -axis), the fluence difference between coated and uncoated particles is plotted for particles of various coating thicknesses (see legend and Table 1 for coating masses corresponding to the condenser temperatures shown in the legend). The y -axis is the shift in fluence between the coated and uncoated curves in Fig. 4

conduction to the surrounding atmosphere, and the amount of energy lost to core-particle sublimation. Equation (13) neglects the latter two effects but demonstrates the influence of these other factors. The deviations from a linear dependence on fluence at high fluences demonstrate the effect of core-particle sublimation. At low to moderate fluences sublimation has little effect on the peak temperature.

At high laser fluences, the maximum temperature and peak LII signal approach a plateau. This plateau region is associated with the fluence range in which the particle has sufficient energy to reach the sublimation temperature of the core particle. Because the sublimation temperature of the core particle should be independent of the coating, we assume that the particles all reach the sublimation temperature at high fluences.

Equation (13) shows that, at any particular laser fluence below the plateau region, T_{\max} decreases with increasing M_{coat} . It follows that the LII signal decreases with increasing coating thickness, which is shown in Figs. 4a and 6a for coating thicknesses up to $\sim 75\%$ by mass (\sim condenser temperature of 85°C). If there is an enhancement in the absorption cross-section σ_{abs} with the particle coating, however, an increase in the first term on the right-hand side of Eq. (13) could compensate for an increase in the second term, and T_{\max} could increase with coating thickness, leading to an increase in peak LII signal with increasing coating thickness and a shift of the

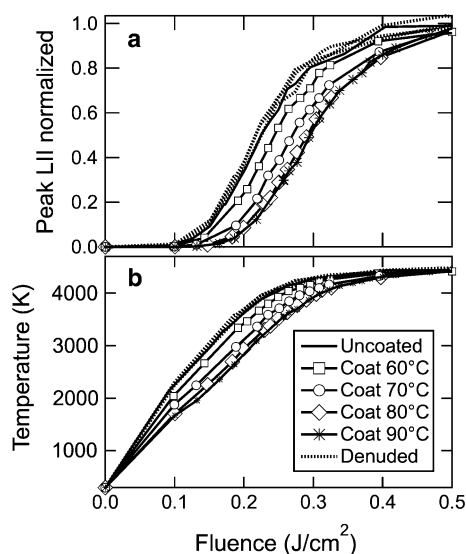


Fig. 6 Fluence dependence of the peak LII signal and maximum particle temperature. **a** The normalized peak of the LII temporal profile is plotted relative to laser fluence on a linear scale for low to moderate coating thickness, as indicated in the legend. **b** This panel shows the maximum particle temperatures corresponding to the data in the *top panel*. Temperatures were calculated using Eq. (8). The coating masses and mass fractions corresponding to the condenser temperatures shown in the legend are given in Table 1. All curves corresponding to the denuded particles are indicated by *dotted lines*

excitation curve to lower fluences. Equation (15) suggests that plotting the fluence for coated particles as a function of the fluence at which the uncoated particles reach the same LII signal level will allow us to separate these effects. Figure 7 shows a series of plots of matching fluences and linear fits to the data, and Table 2 summarizes the results. The data were fit in the range of uncoated fluences of 0.126–0.212 J/cm², which corresponds to normalized peak LII signals between 0.05 and 0.4.

The slopes derived for coated (not denuded) particles are ≥ 1 for all coating thicknesses (Table 2), suggesting that the absorption cross-section is not enhanced by the coatings but may instead be reduced by the coatings. In our experiments, however, the slope is defined by fluences at which particles reach temperatures ($>2,000$ K) well above the boiling point of oleic acid (658.5 K) (Fig. 6b). Under these conditions, coatings may be mostly evaporated in the early part of the laser pulse and thus may not have a significant contribution to the pulse-averaged absorption cross-section. At heavier coating thicknesses, however, which may not be fully vaporized by the laser (as discussed below), the absorption cross-section appears to be substantially reduced by the coating, according to the simple analysis provided by Eq. (17). These effects may be attributable to a reduction in the absorption cross-section caused by restructuring of the coated particle [32, 45, 67].

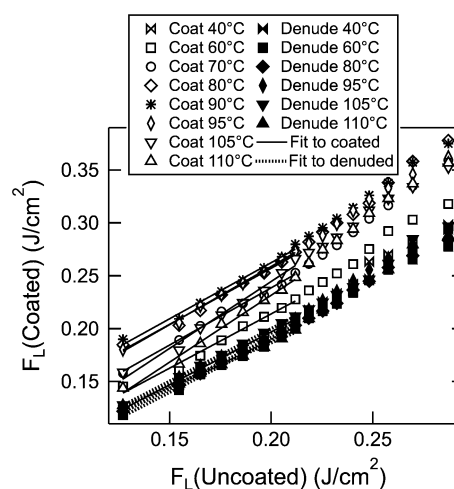


Fig. 7 Correlations of coated and uncoated fluences that lead to the same normalized peak LII signal. The symbols represent data, and the lines represent fits of Eq. (15) to the data for peak LII signal levels between 0.05 and 0.4, which corresponds to uncoated fluences of 0.126–0.212 J/cm². The results of the fits are summarized in Table 2

Table 2 Summary of fits using Eq. (15) to data in Fig. 7

Coating	Slope	Slope uncertainty*	Intercept	Intercept uncertainty*
Very light	1.00	0.01	−0.0033	0.0015
Light	1.03	0.06	0.0089	0.0107
Moderately light	1.08	0.03	0.0224	0.0063
Moderate	1.06	0.05	0.0451	0.0087
Moderately heavy	1.06	0.05	0.0503	0.0087
Heavy	1.10	0.02	0.0391	0.0043
Very heavy	1.27	0.07	−0.0084	0.0125
Extremely heavy	1.26	0.06	−0.0210	0.0099
Very light denuded	0.965	0.010	−0.0012	0.0018
Light denuded	0.984	0.028	−0.0078	0.0050
Moderate denuded	0.959	0.006	−0.0006	0.0011
Heavy denuded	0.940	0.018	0.0079	0.0033
Very heavy denuded	0.993	0.004	0.0015	0.0007
Extremely heavy denuded	0.829	0.018	0.0021	0.0032

* Standard deviation of one σ

We can estimate the amount of coating evaporated by combining the intercept with the slope from the fits in Fig. 7 using Eq. (18). Figure 8 shows a plot of the evaporated coating mass inferred from Eq. (18) as a function of the coating mass on the particles derived from the CPMA measurements published recently [51]. At the lower coating thicknesses (≤ 65 % by mass), the mass evaporated is equal to the measured coating mass, suggesting that all of the coating on the particle is evaporated from the particle during laser heating.

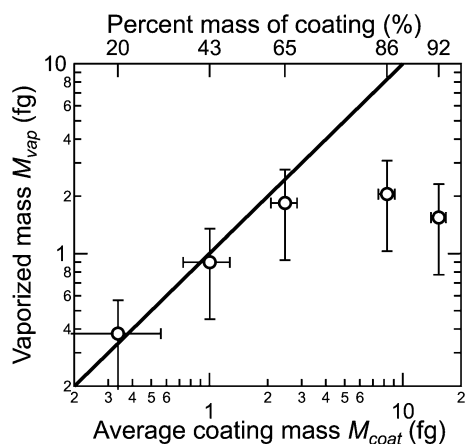


Fig. 8 Mass vaporized by the laser plotted as a function of measured mass of the coating. The evaporated masses M_{vap} were derived from the fits shown in Fig. 7 using Eq. (18), and the coating masses M_{coat} were measured using a CPMA. Error bars for M_{coat} represent 1σ uncertainties of the masses of the coated particles and uncoated core particles. Error bars for M_{vap} are estimated uncertainties associated with the density of polycrystalline graphite and $E(m)$ for uncoated particles. The 1:1 line represents perfect agreement between M_{vap} and M_{coat}

At high coating thicknesses ($>65\%$ by mass), on the other hand, the analysis shown in Fig. 8 suggests that the evaporated mass is significantly less than the coating mass, that is, the laser does not evaporate all of the coating. These results are consistent with conclusions drawn from mobility size distributions of laser-heated coated particles [51]. Examples of these results are shown in Fig. 9. The mobility-diameter size distribution for the original uncoated particles is shown in Fig. 9a to have a median mobility diameter of 152 nm in the main (singly charged) mode. Adding moderate to heavy coatings increases the particle size, as shown for a moderate coating of 65% by mass in Fig. 9a and heavy coatings of over 90% by mass in Fig. 9b, c. Laser heating these particles at a laser fluence of 0.2 J/cm^2 increases the soot core temperature to a little over 3,000 K but causes little change in the main mode of the mobility size distribution for the heavy coatings shown in Fig. 9b, c, suggesting that much of the oleic acid droplet is not vaporized during laser heating. Laser heating the particles with the moderate coating causes a shift to smaller particle sizes. In all cases, some small particles appear in the size distribution. When these particles are sent through the thermodenuder to remove oleic acid, the smallest particles ($< \sim 50 \text{ nm}$) disappear, suggesting that these particles were predominantly recondensed oleic acid droplets generated from oleic acid vaporized from the coated particles during laser heating. Significant numbers of particles in a broad distribution with a median diameter of $\sim 100 \text{ nm}$ are not removed in the thermodenuder. These particles are

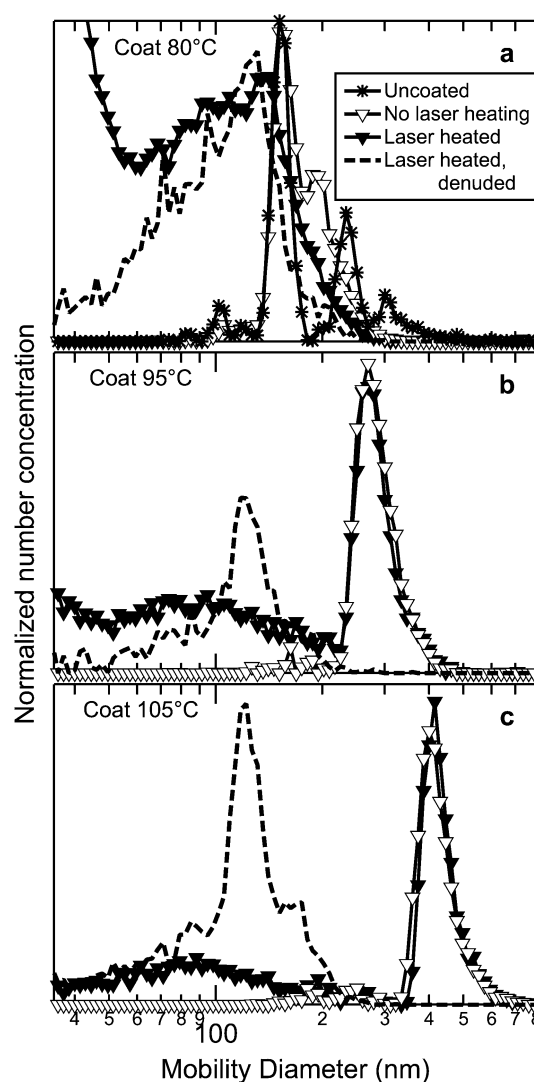


Fig. 9 Mobility-diameter size distributions of laser-heated coated particles. The uncoated particles were size selected with a DMA set to 150 nm. Size distributions are shown for coated particles, laser-heated coated particles, and coated particles heated with the laser and then sent through a denuder for coating thicknesses of **a** 65% by mass, **b** 92% by mass, and **c** 97% by mass. The units on the y-axis are normalized values of number of particles per unit volume in each mobility-size bin ($dW/d\log D_m$). The curves representing particles that have not been laser heated are scaled to the top of the graph, and the other curves are scaled to the non-laser-heated curves

likely fragments of the soot aggregates generated during laser heating. The appearance of these particles prior to the thermodenuder suggests that they are ejected from the particle during laser heating. The majority of the particles, however, are contained within the unvaporized oleic acid droplet until the oleic acid is removed in the thermodenuder at which point the main mode in the size distribution shifts to the size of the soot core. When the moderately coated, laser-heated particles are sent through the thermodenuder, particles disappear between 145 and 200 nm and

a new peak appears between 110 and 140 nm, suggesting that, even under these conditions, some of the core particles are still contained in a mantle of oleic acid. Recent results have shown that increasing the laser fluence leads to more small-particle generation [51], but a large fraction of these small particles are trapped within the unvaporized oleic acid droplet.

This mechanism is different from the mechanism recently proposed by Moteki and Kondo [71] that laser heating causes volatile coatings on soot particles to be explosively desorbed and that explosive vaporization of the coating near the soot particle causes the soot particle to be separated from the volatile coating. Our results indicate that heavily coated soot particles heat and rapidly vaporize some coating during the laser pulse. This rapid vaporization leads to expansion of the aggregate that is forceful enough to expel aggregate fragments and expand the remaining aggregate into a less compact morphology [51]. As shown in Fig. 9, however, only the small fragments tend to separate from the unvaporized oleic acid mantle. For heavily coated particles (>~75 % coating by mass), most of the soot is contained within the oleic acid droplet. The coating-induced fragmentation observed is unlikely to influence LII signals because the primary-particle sizes do not change, and the fragments are relatively large.

Despite the fact that these particles remain inside the oleic acid droplet after laser heating, there is evidence that they reach temperatures high enough to lead to annealing, that is, an increase in ordering of the particle fine structure. Figure 10 shows TEM images of uncoated particles in the left panels and heavily coated particles in the right panels. In the top two panels, the particles have not been laser heated. In the middle panels, they have been heated at a low laser fluence (0.20 J/cm^2), and in the bottom panels, they have been heated at a higher laser fluence (0.27 J/cm^2). Whether coated or not, the particles show evidence of annealing (dark rings around the primary particles) at the higher fluence. This phenomenon has been observed previously for uncoated soot particles at fluences $>0.3 \text{ J/cm}^2$ at $1,064 \text{ nm}$ [14, 43, 96–98]. The images for the lower fluence suggest the start of annealing with some evidence of graphitic sections. This observation is consistent with previous work that showed evidence of small sections of graphitic structure for soot irradiated at 0.24 J/cm^2 at $1,064 \text{ nm}$ but no evidence of the long-range order seen in particles that were irradiated at higher fluence [43].

There is no evidence of coating pyrolysis, polymerization, and/or graphitization of the coating to form new refractory material on the particle. Recent results demonstrate that the core particles do not gain mass when laser heated, whether or not they have been through the thermodeuder prior to laser irradiation [51]. Figure 11 shows mass distributions measured for coated particles that have

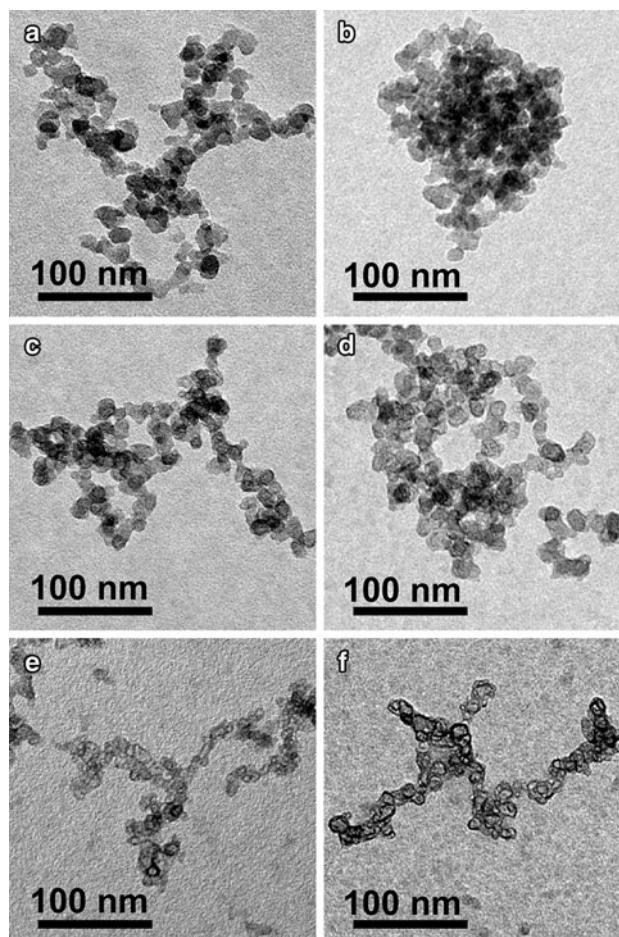


Fig. 10 TEM images of an uncoated and heavily coated soot particles that have been laser heated. Images show **a** an uncoated particle that was not laser heated, **b** a coated particle (95°C coating) that was not laser heated, **c** an uncoated particle laser heated at 0.20 J/cm^2 , **d** a coated particle (95°C coating) laser heated at 0.20 J/cm^2 , **e** an uncoated particle laser heated at 0.27 J/cm^2 , and **f** a coated particle (95°C coating) laser heated at 0.27 J/cm^2 . The scale is indicated in the lower left corner of each panel. The TEM images were recorded at a magnification of 250,000

been laser heated before (Fig. 11a) and after (Fig. 11b) thermal denuding. Figure 11 shows uncoated particles that have been similarly treated and untreated uncoated particles for comparison. At a fluence of 0.2 J/cm^2 , laser heating does not affect the mass distribution of uncoated particles. Figure 11a demonstrates that laser heating coated particles leads to a shift of the distribution to lower masses. This mass shift is caused by aggregate fragmentation, presumably because of rapid vaporization of coatings that forcefully break the particle apart [51]. Such signs of fragmentation are not observed for uncoated particles. Signs of fragmentation are also not apparent for the particles that have been thermally denuded prior to laser heating, as shown in Fig. 11b. Particles that have been denuded and laser heated have the same mass distribution as the

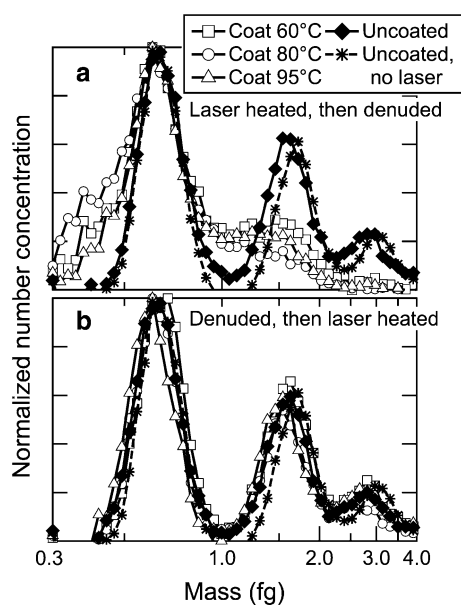


Fig. 11 Mass distributions of coated particles that have been laser heated and thermally denuded. The uncoated particles were size selected with a DMA set to 150 nm. Particles that were not coated were also size selected. The laser fluence was 0.15 J/cm^2 for all particles that were thermally denuded prior to laser heating. Mass distributions are shown for particles that were **a** laser heated and then denuded and **b** thermally denuded and then laser heated. The mass distribution for the uncoated, non-laser-heated particles is the same in both panels. The other uncoated distributions were treated similarly to the coated particles (laser heated and denuded) for comparison. The units on the y-axis are normalized values of number of particles per unit volume in each mass bin ($dN/d\log M$). Curves are scaled to the top of each graph and identified in the legend

uncoated particles. This result is consistent with the hypothesis that rapid vaporization of coatings is responsible for particle morphology change and aggregate fragmentation during laser heating, which cannot occur if the coatings have been removed prior to laser heating.

Figures 4 and 6a show that the denuded particles require no additional laser energy to reach the same LII signals as the uncoated particles and are slightly shifted to lower laser fluences than the uncoated particles, that is, the difference for denuded particles in Fig. 5 is negative. This shift suggests either an enhancement in the absorption cross-section for the denuded particles, thereby requiring a lower laser fluence to heat the particles, or a reduction in the cooling rate for these particles, perhaps as a result of a reduction in the conductive-cooling rate. As indicated by Eq. (17), the inverse values of the slopes given in Table 2 provide an estimate of the enhancement in the absorption cross-sections. These values suggest an enhancement of a few percent for the denuded particles. Restructuring, however, is expected to reduce the absorption cross-section because of shielding effects [32, 45, 67]. A reduction in the

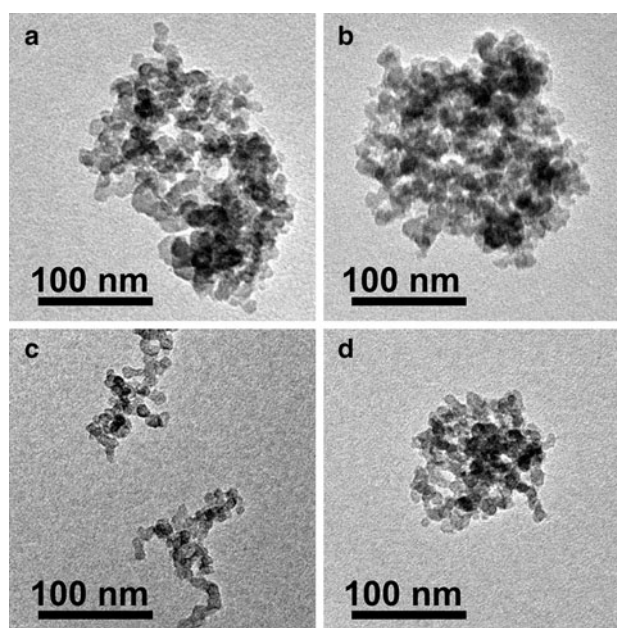


Fig. 12 TEM images of coated, thermally denuded, and laser-heated soot particles. The scale is indicated in each figure. The TEM images were recorded at a magnification of 250,000. The particles were **a** moderately coated with oleic acid, **b** moderately coated and then denuded, **c** moderately coated and then laser heated, **d** moderately coated, denuded and then laser heated. In all cases, the particles were size selected (DMA set to 150 nm) prior to coating

conductive-cooling rate is a likely explanation for this fluence shift and will have the appearance of an enhancement in the absorption cross-section given by the slopes in Table 2. Coating and denuding the particles lead to an irreversible restructuring of the particle that may cause the conductive-cooling rate to be significantly reduced [51]. Figure 10a shows a TEM image of an uncoated particle, which has a typical fractal dimension of 1.8. Figure 12a shows a moderately coated particle (condenser temperature of 80°C). The particle has collapsed and has a fractal dimension of 2.47. When denuded, the particle stays collapsed, as shown in Fig. 12b, even if the particle is laser heated, as shown in Fig. 12d [51]. This collapsed morphology reduces the available surface area for gas-particle collisions and thus reduces the conductive-cooling rate.

4.2 Effects of coatings on the LII temporal profile

Figure 13 shows a comparison of the early portion of the LII temporal profiles for uncoated and coated particles generated at several laser fluences. The laser temporal profile is also shown. All curves are scaled to the top of the graph. During the laser pulse, the black-carbon core of the particles absorbs the 1,064-nm radiation, which leads to an increase in the particle temperature.

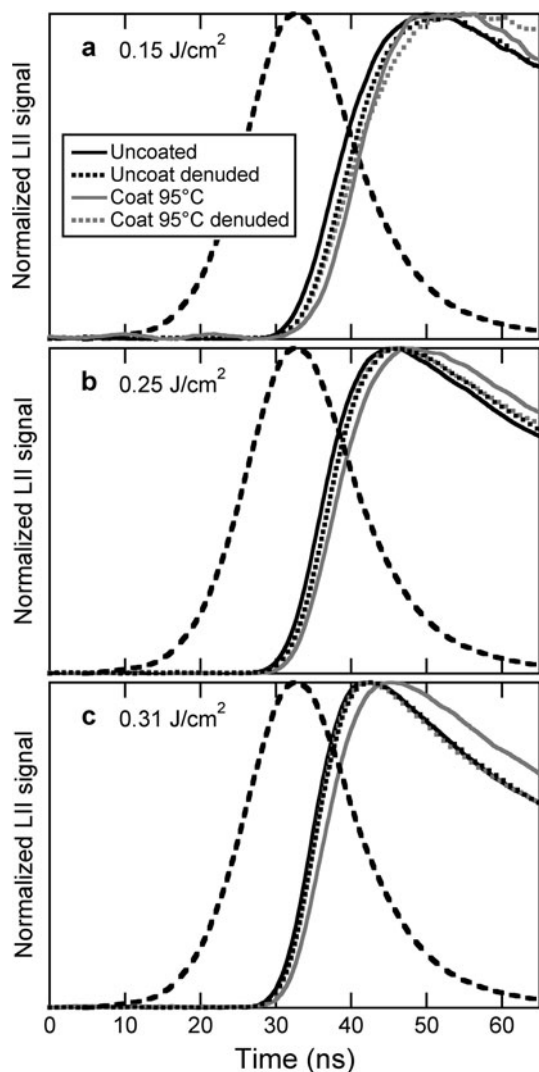


Fig. 13 LII temporal profiles at selected laser fluences for uncoated, coated, and denuded particles. Temporal profiles were recorded at the fluences indicated in the figure for uncoated particles, uncoated particles that were sent through the denuder, particles that were coated at a condenser temperature of 95 °C (coating was 92 % by mass) and similarly coated and denuded. The laser temporal profile is indicated by the *dashed line* in each panel

At low laser fluences, the particle reaches its maximum temperature and, hence, emits its maximum signal, at the point near the end of the laser pulse when the absorptive-heating rate is balanced by the conductive-cooling rate. In Fig. 13a, the peak signal for the uncoated and coated particles occurs at ~ 50 ns, whereas the peak in the signal for the thermally denuded particles occurs a little later at ~ 54 ns. This shift in time is likely attributable to a lower conductive-cooling rate because of the particle restructuring and the corresponding decrease in the effective surface area. The balance in conductive-cooling rate and absorptive-heating rate thus occurs later in the laser pulse. This result is consistent with the shift in the peak LII curves to

lower fluences for denuded particles relative to uncoated particles observed in Fig. 3. The effect is also seen as a negative fluence difference in Fig. 4. The temporal peaks for the coated particles are comparable to those of the uncoated particles. Although the coated particles initially have a similar restructured morphology, laser heating removes the coating in such a way that the particles return to a less compact morphology (as shown in Fig. 12c), and the conductive-cooling rate is thus comparable to that of the uncoated particle.

At all laser fluences, there is a delay in the rising edge of the LII signal for the coated particles relative to the uncoated particles. This delay is attributable to the additional time needed to vaporize the volatile coating before the temperature of the particle core can increase sufficiently to produce incandescence. This delay is expected to increase with particle coating thickness [50, 71] and with increasing specific heat and enthalpy of vaporization of the coating. The optical properties of the coating will also influence this delay; a coating that increases the absorption cross-section and absorptive-heating rate will cause the particles to heat faster and will decrease the delay. In addition, particle restructuring is likely to decrease the absorption cross-section because of shielding effects [32, 45, 67], and thus, the propensity of the coating to cause restructuring should increase this coating-induced delay. This reduction in the absorption cross-section caused by restructuring is a possible explanation for the delay in signal observed for the denuded particles and shown in Fig. 13. Alternatively, the delay observed for the denuded particles could be caused by a modification to the optical properties of the core particle caused by time spent at elevated temperatures in the thermodenuder. Partial annealing of the particle may lead to a reduction in the absorption cross-section, for example [93, 99–101]. This explanation is consistent with the observation that the uncoated particles sent through the denuder have rise times that are nearly identical to those of the denuded coated particles, but the “denuded” uncoated particles do not demonstrate the restructuring observed for the denuded coated particles.

In addition to the strong dependence on temperature, the LII signal also depends on particle diameter (d_p) and scales as d_p^3 . At laser fluences high enough to heat particles to the sublimation point of the black-carbon core, evaporative cooling and mass loss cause the peak signal to move to earlier times. An example is shown in Fig. 13. At a fluence of ~ 0.15 J/cm² (Fig. 13a), the signal for uncoated particles reaches a peak at ~ 50 ns, whereas the peak signal occurs at ~ 41 ns at ~ 0.30 J/cm² (Fig. 13c). At even higher fluences, the signal can reach a maximum before the peak in the laser pulse.

Figure 14 compares temporal profiles for fluences at which uncoated, coated, and denuded particles reached the

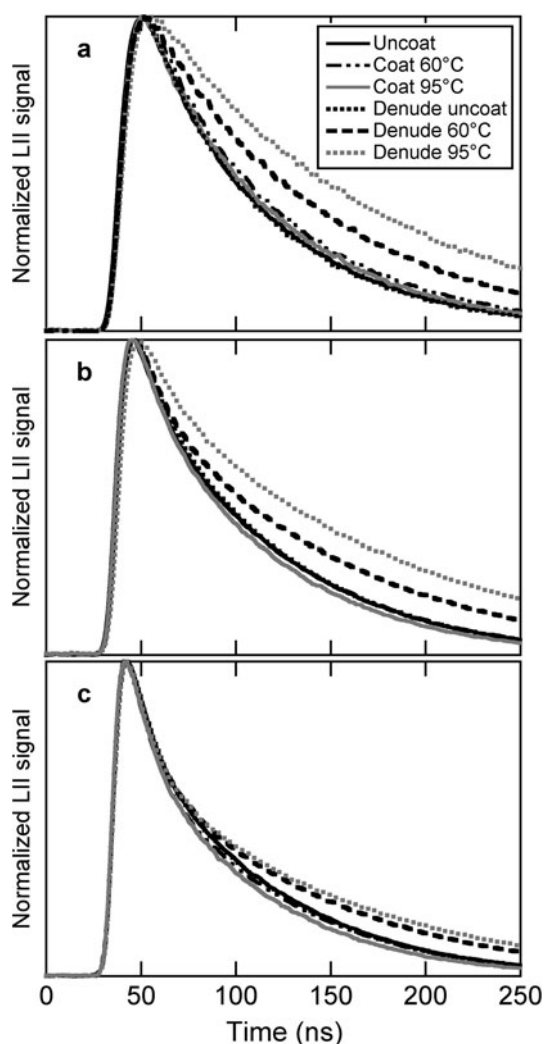


Fig. 14 LII temporal profiles at selected LII signal levels for coated and uncoated particles. Temporal profiles in each panel were recorded at fluences that gave the same LII peak signal. Profiles were recorded for particles that were uncoated, uncoated and then sent through the denuder, coated at a condenser temperature of 60 °C (coating was 20 % by mass) or 95 °C (coating was 92 % by mass), and similarly coated and denuded. The fluences used were **a** 0.15 J/cm² for the uncoated and denuded particles, 0.18 J/cm² for the 60 °C coating, and 0.21 J/cm² for the 95 °C coating, **b** 0.25 J/cm² for the uncoated and denuded particles, 0.28 J/cm² for the 60 °C coating, and 0.31 J/cm² for the 95 °C coating, and **c** 0.31 J/cm² for the uncoated and denuded particles, 0.34 J/cm² for the 60 °C coating, and 0.37 J/cm² for the 95 °C coating

same peak temperature and LII signal, that is, the same y value on Fig. 3. All curves are scaled to the top of the graph in each panel. Such plots provide information about the conductive-cooling rates and evaporative mass loss rates of the laser-heated particles. At the lowest fluence range (Fig. 14a), the decay curves for the coated and uncoated particles are generally independent of coating. This result indicates that, once the particle coating has been vaporized by the laser, the conductive-cooling rate is

independent of whether the particle had been coated. The denuded particles, on the other hand, have very different signal decay rates. This result suggests that the conductive-cooling rate is significantly reduced for the restructured denuded particles. This explanation is consistent with the observation that the effect is more significant for the heavily coated and denuded particles than for the lightly coated and denuded particles; the lightly coated, denuded particles are less collapsed than the heavily coated, denuded particles, as we have recently demonstrated [51]. Whereas laser vaporization of the coating returns the particles to a less compact morphology, laser heating of the denuded particles does not, and the resulting reduction in effective particle surface area of the restructured particles significantly reduces the conductive-cooling rate. This effect is also seen at higher fluences, such as those shown in Fig. 14b. During the laser pulse, however, the signal decay is dominated by evaporative mass loss, which is comparable for all of the particles, whether uncoated, coated, or denuded, as shown in Fig. 14b, c.

5 Summary and conclusions

The magnitude of the LII signal is very sensitive to coating thickness at fluences below 0.4 J/cm². Signals decrease with increasing coating thickness up to a thickness of ~75 % by mass. This effect is attributable to the additional energy needed to vaporize the coating in addition to heating the particle to incandescence temperatures. At higher coating thickness, signals increase with increasing coating thickness. This behavior does not appear to be attributable to an increase in the absorption cross-section with coating thickness at high coating thicknesses. At these coating thicknesses, the coating is not fully vaporized. Although some small fragments are ejected from the mantle of unvaporized oleic acid, a majority of the particles are contained within the remaining oleic acid droplet after laser heating. Denuded particles have slightly higher signals at these fluences; this behavior is likely attributable to the reduced conductive-cooling rate because of the irreversible restructuring of the particle in the thermodenuder.

The delay in the onset of the LII signal appears to depend on a range of factors, including coating thickness, coating-induced particle morphology changes, and optical-property changes caused by coating and heating in a thermodenuder. We also expect that other physical characteristics of the coatings, such as the enthalpy of vaporization and density, will influence this signal delay. In addition, the signal decay rates appear to be very sensitive to the irreversible restructuring of particles processed in a thermodenuder. The resulting morphology change reduces the exposed surface area, conductive-

cooling rate, and LII signal decay rates substantially. Particles that have been coated and not thermally denuded prior to laser heating return to a less compact morphology during the laser pulse and have very similar LII decay rates to uncoated particles.

Acknowledgments We thank Daniel Strong for the renditions of the experimental setup shown in Fig. 1. We are very grateful to Chris Sorensen for his advice on analysis of the TEM images, Jeff Headrick for his assistance with the TEM image analysis, and Alexei Khalizov for his insightful comments about soot restructuring. This work was funded by the Sandia Laboratory Directed Research and Development program. The TEM analysis, the thermodenuder design, construction, and testing, and the CPMA were funded by the Division of Chemical Sciences, Geosciences, and Biosciences, the Office of Basic Energy Sciences, the US Department of Energy. Sandia is a multi-program laboratory operated by Sandia Corporation, a Lockheed Martin Company, for the National Nuclear Security Administration under contract DE-AC04-94-AL85000.

Open Access This article is distributed under the terms of the Creative Commons Attribution License which permits any use, distribution, and reproduction in any medium, provided the original author(s) and the source are credited.

References

- IPCC Climate Change 2007: The physical science basis. Contribution of Working Group I to the fourth assessment report of the intergovernmental panel on climate change, Cambridge University Press, Cambridge, 2007
- S.E. Bauer, S. Menon, D. Koch, T.C. Bond, K. Tsigaridis, *Atmos. Chem. Phys.* **10**, 7439 (2010)
- D. Shindell, J.C.I. Kuylenstierna, E. Vignati, R. van Dingenen, M. Amann, Z. Klimont, S.C. Anenberg, N. Müller, G. Janssens-Maenhout, F. Raes, J. Schwartz, G. Faluvegi, L. Pozzoli, V. Ramanathan, K. Hicks, N.T.K. Oanh, G. Milly, M. Williams, V. Demkine, D. Fowler, *Science* **335**, 183 (2012)
- J.E. Dec, A.O. zur Loye, D.L. Siebers, *SAE Trans.* **100**(3), 277 (1991)
- J.A. Pinson, D.L. Mitchell, R.J. Santoro, *Proc. SAE SAE Paper No. 932650* (1993)
- H. Fujimoto, K. Kurata, G. Asai, J. Senda, *Proc. SAE SAE Paper No. 982630* (1998)
- K. Inagaki, S. Takasu, K. Nakakita, *SAE Trans.* **108**(3), 574 (1999)
- D. Hertler, R. Stirn, S. Arndt, R. Grzeszik, A. Dreizler, *Appl. Phys. B* **104**, 399 (2011)
- B.F. Kock, B. Tribalet, C. Schulz, P. Roth, *Combust. Flame* **147**, 79 (2006)
- H. Zhao, N. Ladommatos, *Prog. Energy Combust. Sci.* **24**, 221 (1998)
- N.P. Tait, D.A. Greenhalgh, *Ber. Bunsenges. Phys. Chem.* **97**, 1619 (1993)
- C. Allouis, A. D'Alessio, C. Noviello, F. Beretta, *Combust. Sci. Technol.* **153**, 51 (2000)
- B. Axelsson, R. Collin, P.-E. Bengtsson, *Appl. Opt.* **39**, 3683 (2000)
- R.L. Vander Wal, T.M. Ticich, A.B. Stephens, *Appl. Phys. B* **67**, 115 (1998)
- F. Cignoli, S. Benecchi, G. Zizak, *Appl. Opt.* **33**, 5778 (1994)
- C.R. Shaddix, K.C. Smyth, *Combust. Flame* **99**, 723 (1994)
- D. Snelling, K.A. Thomson, G.J. Smallwood, Ö.L. Gülder, *Appl. Opt.* **38**, 2478 (1999)
- P.O. Witze, R.E. Chase, M.M. Maricq, D.H. Podsiadlik, N. Xu, *Proc. SAE* (2004)
- J. Delhay, P. Desgroux, E. Therssen, H. Bladh, P.-E. Bengtsson, H. Hönen, J.D. Black, I. Vallet, *Appl. Phys. B* **95**, 825 (2009)
- M.P. Johnson, M. Hilton, D.R. Waterman, J.D. Black, *Meas. Sci. Technol.* **14**, 1146 (2003)
- P.O. Witze, M. Gershenzon, H.A. Michelsen, *Proc. SAE SAE Paper no.* (2005)
- J. Liggio, M. Gordon, G.J. Smallwood, S.-M. Li, C. Stroud, R. Staebler, G. Lu, P. Lee, B. Taylor, J.R. Brook, *Environ. Sci. Technol.* **46**, 4819 (2012)
- A.J. Sedlacek III, E.R. Lewis, L. Kleinman, J. Xu, Q. Zhang, *Geophys. Res. Lett.* **39**, L06802 (2012)
- J.P. Schwarz, R.S. Gao, D.W. Fahey, D.S. Thomson, L.A. Watts, J.C. Wilson, J.M. Reeves, M. Darbehshti, D.G. Baumgardner, G.L. Kok, S.H. Chung, M. Schulz, J. Hendricks, A. Lauer, B. Kärcher, J.G. Slowik, K.H. Rosenlof, T.L. Thompson, A.O. Langford, M. Loewenstein, K.C. Aikin, *J. Geophys. Res.* **111**, D16207 (2006)
- R. Subramanian, G.L. Kok, D.G. Baumgardner, A. Clarke, Y. Shinozuka, T.L. Campos, C.G. Heizer, B.B. Stephens, B. de Foy, P.B. Voss, R.A. Zaveri, *Atmos. Chem. Phys.* **10**, 219 (2010)
- M.R. Canagaratna, J.T. Jayne, J.-L. Jimenez, J.D. Allan, M.R. Alfarra, O. Zhang, T.B. Onasch, F. Drewnick, H. Coe, A.M. Middlebrook, A. Della, L.R. Williams, A.M. Trimborn, M.J. Northway, P.F. DeCarlo, C.E. Kolb, P. Davidovits, D.R. Worsnop, *Mass Spectrom. Rev.* **26**, 185 (2007)
- D.G. Baumgardner, G. Kok, G. Raga, *Geophys. Res. Lett.* **31**, L06117 (2004)
- G.R. McMeeking, T. Hamburger, D. Liu, M. Flynn, W.T. Morgan, M.J. Northway, E.J. Highwood, R. Krejcar, J.D. Allan, A. Minikin, H. Coe, *Atmos. Chem. Phys.* **10**, 9393 (2010)
- A.R. Metcalf, J.S. Craven, J.J. Ensberg, J. Brioude, W. Angevine, A. Sorooshian, H.T. Duong, H.H. Jonsson, R.C. Flagan, J.H. Seinfeld, *J. Geophys. Res.* **117**, DO0V13 (2012)
- C. Schulz, B.F. Kock, M. Hofmann, H.A. Michelsen, S. Will, B. Bougie, R. Suntz, G.J. Smallwood, *Appl. Phys. B* **83**, 333 (2006)
- R.W. Fenn, H. Oser, *Appl. Opt.* **4**, 1504 (1965)
- K.N. Liou, Y. Takano, P. Yang, *J. Quant. Spectrosc. Radiat. Transfer* **112**, 1581 (2011)
- T.P. Ackerman, O.B. Toon, *Appl. Opt.* **20**, 3661 (1981)
- M.Z. Jacobson, *Geophys. Res. Lett.* **27**, 217 (2000)
- K.A. Fuller, W.C. Malm, S.M. Kreidenweis, *J. Geophys. Res.* **104**, 15 (1999)
- B. Stout, C. Andraud, S. Stout, J. Lafait, *J. Opt. Soc. Am. A* **20**, 1050 (2003)
- T.C. Bond, G. Habib, R.W. Bergstrom, *J. Geophys. Res.* **111**, D20211 (2006)
- D.A. Lack, C.D. Cappa, *Atmos. Chem. Phys.* **10**, 4207 (2010)
- C.D. Cappa, T.B. Onasch, P. Massoli, D.R. Worsnop, T.S. Bates, E.S. Cross, P. Davidovits, J. Hakala, K.L. Hayden, B.T. Jobson, K.R. Kolesar, D.A. Lack, B.M. Lerner, S.-M. Li, D. Mellon, I. Nuaaman, J.S. Olfert, T. Petäjä, P.K. Quinn, C. Song, R. Subramanian, E.J. Williams, R.A. Zaveri, *Science* **337**, 1078 (2012)
- K. Park, D.B. Kittelson, P.H. McMurry, *Aerosol Sci. Technol.* **38**, 881 (2004)
- Ü.Ö. Köylü, G.M. Faeth, *Combust. Flame* **89**, 140 (1992)
- B. Hu, B. Yang, Ü.Ö. Köylü, *Combust. Flame* **134**, 93 (2003)
- H.A. Michelsen, A.V. Tivanski, M.K. Gilles, L.H. van Poppel, M.A. Dansson, P.R. Buseck, *Appl. Opt.* **46**, 959 (2007)
- Ü.Ö. Köylü, G.M. Faeth, *Combust. Flame* **100**, 621 (1995)

45. C.M. Sorensen, *Aerosol Sci. Technol.* **35**, 648 (2001)
46. T.T. Charalampopoulos, H. Chang, *Combust. Flame* **87**, 89 (1991)
47. Ü.Ö. Köylü, Y.C. Xing, D.E. Rosner, *Langmuir* **11**, 4848 (1995)
48. E.F. Mikhailov, S.S. Vlasenko, L. Krämer, R. Niessner, *J. Aerosol Sci.* **32**, 697 (2001)
49. I. Colbeck, L. Appleby, E.J. Hardman, R.M. Harrison, *J. Aerosol Sci.* **21**, 527 (1990)
50. J.G. Slowik, E.S. Cross, J.-H. Han, P. Davidovits, T.B. Onasch, J.T. Jayne, L.R. Williams, M.R. Canagaratna, D.R. Worsnop, R.K. Chakrabarty, H. Moosmüller, W.P. Arnott, J.P. Schwarz, R.-S. Gao, D.W. Fahey, G.L. Kok, A. Petzold, *Aerosol Sci. Technol.* **41**, 295 (2007)
51. R.P. Bambha, M.A. Dansson, P.E. Schrader, H.A. Michelsen, Carbon submitted (2012)
52. S. Kütz, A. Schmidt-Ott, *J. Aerosol Sci.* **23**, S357 (1992)
53. B. Miljevic, N.C. Surawski, T. Bostrom, Z.D. Ristovski, *J. Aerosol Sci.* **47**, 48 (2012)
54. H. Saathoff, K.-H. Naumann, M. Schnaiter, W. Schöck, O. Möhler, U. Schurath, E. Weingartner, M. Gysel, U. Baltensperger, *J. Aerosol Sci.* **34**, 1297 (2003)
55. H. Xue, A.F. Khalizov, L. Wang, J. Zheng, R. Zhang, *Environ. Sci. Technol.* **43**, 2787 (2009)
56. E.S. Cross, T.B. Onasch, A. Ahern, W. Wrobel, J.G. Slowik, J. Olfert, D.A. Lack, P. Massoli, C.D. Cappa, J.P. Schwarz, J.R. Spackman, D.W. Fahey, A. Sedlacek, A.M. Trimborn, J.T. Jayne, A. Freedman, L.R. Williams, N.L. Ng, C. Mazzoleni, M. Dubey, B. Brem, G. Kok, R. Subramanian, S. Freitag, A. Clarke, D. Thornhill, L.C. Marr, C.E. Kolb, D.R. Worsnop, P. Davidovits, *Aerosol Sci. Technol.* **44**, 592 (2010)
57. M.T. Spencer, K.A. Prather, *Aerosol Sci. Technol.* **40**, 585 (2006)
58. Z. Lu, J. Hao, L. Hu, H. Takekawa, *J. Aerosol Sci.* **39**, 897 (2008)
59. P.A. Bueno, D.K. Havey, G.W. Mulholland, J.T. Hodges, K.A. Gillis, R.R. Dickerson, M.R. Zachariah, *Aerosol Sci. Technol.* **45**, 1217 (2011)
60. R. Ghazi, J.S. Olfert, *Aerosol Sci. Technol.* **47**, 192 (2013)
61. J.G. Slowik, E.S. Cross, J.-H. Han, J. Kolucki, P. Davidovits, L.R. Williams, T.B. Onasch, J.T. Jayne, C.E. Kolb, D.R. Worsnop, *Aerosol Sci. Technol.* **41**, (2007)
62. R. Zhang, A.F. Khalizov, J. Pagels, D. Zhang, H. Xue, P.H. McMurry, *Proc. Natl. Acad. Sci. USA.* **105**, 10291 (2008)
63. A.F. Khalizov, H. Xue, L. Wang, J. Zheng, R. Zhang, *J. Phys. Chem.* **113**, 1066 (2009)
64. J. Pagels, A.F. Khalizov, P.H. McMurry, R. Zhang, *Aerosol Sci. Technol.* **43**, 629 (2009)
65. L. Liu, M.I. Mishchenko, W.P. Arnott, *J. Quant. Spectrosc. Radiat. Transfer* **109**, 2656 (2008)
66. J. Frey, J.J. Pinvidic, R. Botet, R. Jullien, *J. de Physique France* **49**, 1969 (1988)
67. D.W. Mackowski, *Appl. Opt.* **34**, 3535 (1995)
68. D.W. Mackowski, *J. Quant. Spectrosc. Radiat. Transfer* **100**, 237 (2006)
69. M. Schnaiter, H. Horvath, O. Möhler, K.-H. Naumann, H. Saathoff, O.W. Schöck, *J. Aerosol Sci.* **34**, 1421 (2003)
70. M. Gangl, J. Kocifaj, G. Videen, H. Horvath, *Atmos. Environ.* **42**, 2571 (2008)
71. N. Moteki, Y. Kondo, *Aerosol Sci. Technol.* **41**, 398 (2007)
72. H.A. Michelsen, F. Liu, B.F. Kock, H. Bladh, A. Boiarciuc, M. Charwath, T. Dreier, R. Hadeif, M. Hofmann, J. Reimann, S. Will, P.-E. Bengtsson, H. Bockhorn, F. Foucher, K.P. Geigle, C. Mounaim-Rousselle, C. Schulz, R. Stirn, B. Tribalet, R. Suntz, *Appl. Phys. B* **87**, 503 (2007)
73. M. Gershenzon, P.O. Witze, H.A. Michelsen, Effect of coatings on laser induced incandescence (LII) of soot, in: American Geophysical Union, Fall Meeting 2004, San Francisco, 2004, pp. Abstract #A31C
74. J.P. Schwarz, J.R. Spackman, R.S. Gao, A.E. Perring, E.S. Cross, T.B. Onasch, A. Ahern, W. Wrobel, P. Davidovits, J. Olfert, M.K. Dubey, C. Mazzoleni, D.W. Fahey, *Aerosol Sci. Technol.* **44**, 612 (2010)
75. F. Liu, G.J. Smallwood, D.R. Snelling, *J. Quant. Spectrosc. Radiat. Transfer* **93**, 301 (2005)
76. F. Liu, M. Yang, F.A. Hill, D.R. Snelling, G.J. Smallwood, *Appl. Phys. B* **83**, 383 (2006)
77. H. Bladh, J. Johnsson, J. Rissler, H. Abdulhamid, N.-E. Olofsson, M. Sanati, J. Pagels, P.-E. Bengtsson, *Appl. Phys. B* **104**, 331 (2011)
78. H. Bladh, J. Johnsson, P.-E. Bengtsson, *Appl. Phys. B* **90**, 109 (2008)
79. S.-A. Kuhlmann, J. Reimann, S. Will, *J. Aerosol Sci.* **37**, 1696 (2006)
80. F. Liu, G.J. Smallwood, *J. Quant. Spectrosc. Radiat. Transfer* **111**, 302 (2010)
81. F. Liu, G.J. Smallwood, *Appl. Phys. B* **104**, 343 (2011)
82. H.A. Michelsen, P.O. Witze, D. Kayes, S. Hochgreb, *Appl. Opt.* **42**, 5577 (2003)
83. J.M. Headrick, F. Goulay, P.E. Schrader, H.A. Michelsen, *Appl. Phys. B* **104**, 439 (2011)
84. M. Fierz, M.G.C. Vernooij, H. Burtscher, *J. Aerosol Sci.* **38**, 1163 (2007)
85. E.O. Knutson, K.T. Whitby, *J. Aerosol Sci.* **6**, 453 (1975)
86. T.C. Williams, C.R. Shaddix, K.A. Jensen, J.M. Suo-Anttila, *Int. J. Heat Mass Transfer* **50**, 1616 (2007)
87. H. Chang, T.T. Charalampopoulos, *Proc. R. Soc. Lond. A* **430**, 577 (1990)
88. Ü.Ö. Köylü, G.M. Faeth, *J. Heat Transfer* **118**, 415 (1996)
89. S.S. Krishnan, K.-C. Lin, G.M. Faeth, *J. Heat Transfer* **123**, 331 (2001)
90. D.R. Snelling, F. Liu, G.J. Smallwood, Ö.L. Gülder, *Combust. Flame* **136**, 180 (2004)
91. H.A. Michelsen, P.E. Schrader, F. Goulay, *Carbon* **48**, 2175 (2010)
92. J. Yon, R. Lemaire, E. Therssen, P. Desgroux, A. Coppalle, K.F. Ren, *Appl. Phys. B* **104**, 253 (2011)
93. H.A. Michelsen, *J. Chem. Phys.* **118**, 7012 (2003)
94. F. Goulay, P.E. Schrader, X. López-Yglesias, H.A. Michelsen, *Appl. Phys. B* submitted (2012)
95. C.D. Cappa, E.R. Lovejoy, A.R. Ravishankara, *J. Phys. Chem. A* **112**, 3959 (2008)
96. R.L. Vander Wal, C.Y. Choi, K.O. Lee, *Combust. Flame* **102**, 200 (1995)
97. R.L. Vander Wal, K.A. Jensen, *Appl. Opt.* **37**, 1607 (1998)
98. R.L. Vander Wal, M.Y. Choi, *Carbon* **37**, 231 (1999)
99. W.A. de Heer, D. Ugarte, *Chem. Phys. Lett.* **207**, 480 (1993)
100. P. Fedorko, V. Skákalová, O. Foltim, F. Kolenic, V. Smatko, *Mater. Sci. Forum* **191**, 171 (1995)
101. B. Michel, T. Henning, C. Jäger, U. Kriebig, *Carbon* **37**, 391 (1999)